ARTICLE

Physical realization of topological Roman surface by spin-induced ferroelectric polarization in cubic lattice

Guangxiu Liu[1,2,6], Maocai Pi[3,4,6], Long Zhou[1], Zhehong Liu[1,2], Xudong Shen[1,5], Xubin Ye [1,2], Shijun Qin [1,2], Xinrun Mi[3,4], Xue Chen[3,4], Lin Zhao[1,2], Bowen Zhou[1,2], Jia Guo[1,2], Xiaohui Yu[1,2], Yisheng Chai [3,4✉], Hongming Weng [1,2,5✉] & Youwen Long [1,2,5✉]

Topology, an important branch of mathematics, is an ideal theoretical tool to describe topological states and phase transitions. Many topological concepts have found their physical entities in real or reciprocal spaces identified by topological invariants, which are usually defined on orientable surfaces, such as torus and sphere. It is natural to investigate the possible physical realization of more intriguing non-orientable surfaces. Herein, we show that the set of spin-induced ferroelectric polarizations in cubic perovskite oxides $AMn_3Cr_4O_{12}$ (A = La and Tb) reside on the topological Roman surface—a non-orientable two-dimensional manifold formed by sewing a Möbius strip edge to that of a disc. The induced polarization may travel in a loop along the non-orientable Möbius strip or orientable disc, depending on the spin evolution as controlled by an external magnetic field. Experimentally, the periodicity of polarization can be the same or twice that of the rotating magnetic field, which is consistent with the orientability of the disc and the Möbius strip, respectively. This path-dependent topological magnetoelectric effect presents a way to detect the global geometry of a surface and deepens our understanding of topology in both mathematics and physics.

---

[1] Beijing National Laboratory for Condensed Matter Physics, Institute of Physics, Chinese Academy of Sciences, Beijing, China. [2] School of Physical Sciences, University of Chinese Academy of Sciences, Beijing, China. [3] Center of Quantum Materials and Devices, Chongqing University, Chongqing, China. [4] Low Temperature Physics Laboratory and Chongqing Key Laboratory of Soft Condensed Matter Physics and Smart Materials, College of Physics, Chongqing University, Chongqing, China. [5] Songshan Lake Materials Laboratory, Dongguan, Guangdong, China. [6] These authors contributed equally: Guangxiu Liu, Maocai Pi. ✉email: yschai@cqu.edu.cn; hmweng@iphy.ac.cn; ywlong@iphy.ac.cn

opological physics is one of the most successful integrations of the mathematics and physics field. As one of the branches of pure mathematics, topology has recently been employed to describe and understand many intriguing physical phenomena, such as the quantum Hall effect[1,2], topological insulators, topological semimetals, and topological superconductors[3–5]. These topological electronic states are classified by various topological invariants, such as the Chern number N, topological classes Z_2 and Z_4, and Euler class χ[6–11]. It is known that the Chern number is defined as the integral of the vector field, i.e., the Berry curvature over the first Brillouin zone of a two-dimensional (2D) periodic system, which is considered as a torus ($\mathbf{T^2}$) and serves as the base manifold. Meanwhile, the magnetic spins and electric dipoles in real space can form topological objects or defects such as skyrmions[12,13], polar skyrmions[14], and polar merons[15]. These can be identified with an integer winding number[16] based on the field of spin or electrical dipole orientations over the base manifold of a sphere ($\mathbf{S^2}$). In this sense, topological invariants are global characteristics, and topology-related physical properties are typically robust against perturbations[3,4,8].

In addition to torus and sphere, there are three other fundamental 2D manifolds found in algebraic topology (see Supplementary Table 1): the Möbius strip, Klein bottle, and Roman surface. The torus and sphere are orientable and have two sides. The Berry curvature flux enclosed by them can be a nonzero quantized value and taken as a topological invariant, such as the Chern number. By contrast, the Möbius strip, Klein bottle, and Roman surface are non-orientable surfaces with only one side. The flux of any vector field through them is zero. A well-known example is that a one-sided Klein bottle cannot be filled with water, but a two-sided bottle can. Moreover, the non-orientable surfaces feature a geometrical property in which a body can be mirror-reflected when traveling along a special loop path on the surface, such as along the Möbius strip without crossing the boundary, and recovers after the second loop of travel. It will be intriguing to realize a physical system that can evolve globally on a non-orientable surface to reflect such unique geometrical properties.

In real space, a Möbius strip with a single boundary has been visualized in nanocrystal/DNA bands[17,18]. Möbius insulators have been proposed and realized in the reciprocal spaces of electronic[19–21] and acoustic crystals[22,23]. Under proper nonsymmorphic symmetry or projective translation symmetry, the Bloch wavefunctions of its boundary states have 4π periodicity instead of 2π, which mimics characteristics of a Möbius strip. Recently, nonorientability has been regarded as a Z_2 gauge charge to describe the topological defect of shear deformation on a Möbius strip[24]. However, the smooth and global evolution of a physical quantity on a non-orientable surface and the detection of its intrinsic geometry remains a challenge. Furthermore, a non-orientable 2D surface without a boundary must self-intersect in a three-dimensional (3D) space, as shown by the Klein bottle[25] (one-sided bottle) and Roman surface[26] ($\mathbf{RP^2}$, real projective plane). This inhibits the physical realization and exhibition of topological behaviors in a 3D real space. Therefore, it is natural to ask whether the Roman surface, the simplest non-orientable 2D manifold without a boundary, can be realized by some physical entity and whether it can demonstrate exotic topological properties or phenomena.

Jakob Steiner discovered and named the Roman surface during his visit to Rome in early 1844. It is composed of a Möbius strip sewed to the edge of a disc and has a high tetrahedral T_d symmetry, which is different from other non-orientable 2D surfaces. Three self-intersecting double lines D_i ($i = a$, b, and c are three mutually perpendicular Cartesian axes) form a right trihedron in a Euclidean 3D phase space. Each double line ends with two pinch points, and they all intersect at the triple point (see Fig. 1 and Supplementary Fig. 1).

The triple point on the Roman surface indicates the intersection of the three surfaces. The analytical equation of the Roman surface $\mathbf{RP^2}$ in mathematics is

$$x^2 y^2 + x^2 z^2 + y^2 z^2 - \delta xyz = 0 \tag{1}$$

where δ is a constant and (x, y, z) is a point in the a, b, and c coordinate systems. As a 2D manifold, there are three types of fundamental closed loops on a Roman surface, and other closed loops are formed by their combination. As Fig. 1c shows, the first type of loop is a red loop that passes through at least one point twice (e.g., this point can be the triple point). It winds twice to close the path on this non-orientable surface because it rides on the Möbius strip, which is a component of the Roman surface. The other two types of loops are blue and green. They are topologically different from the red ones because they do not pass any point twice and wind once to close the path. The blue loop can only wind along one of the double lines D_i ($i = a$, b, c) by $W_i = 1$ time. The green loop does not enclose any double lines and is topologically trivial. The physical entity that matches Eq. (1) may provide an opportunity to realize a Roman surface and exhibit path-dependent properties. Therefore, realizing the Roman surface is intriguing and may extend the territory in the field of topological physics.

Magnetoelectric (ME) multiferroics with spin-induced ferroelectric polarization ($\mathbf{P}$) have received considerable attention owing to their coupled spin and electrical dipole orders[27], where the electric polarization is switched using a magnetic field ($\mathbf{B}$), and the magnetization ($\mathbf{M}$) is switched using an electric field ($\mathbf{E}$)[27,28], giving rise to significant ME effects. A few physical mechanisms have been proposed for ME multiferroics[29–32], providing a fertile and unique playground for investigating
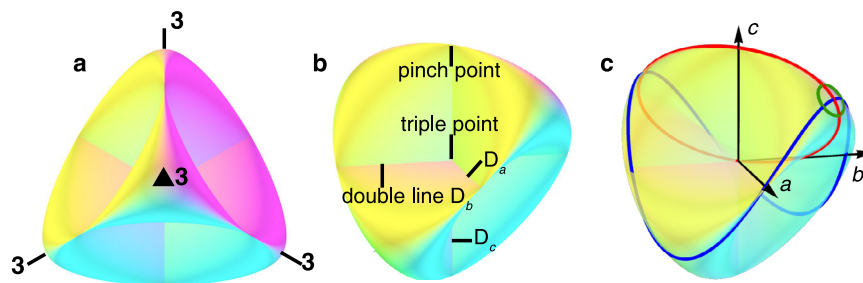
Fig. 1 Schematic diagram of a Roman surface. a, **b** Roman surface with four three-fold axes (**3**), one triple point, six pinch points, and three double lines (D_a, D_b, D_c). **c** Three geometrically different fundamental loops on a Roman surface. The red loop effectively winds twice to pass the two sides of the triple point as it rides on the Möbius strip being part of the Roman surface. The blue loop winds around the double line D_c once to have $W_c = 1$. The green loop does not enclose any double lines with zero W_i ($i = a$, b, c). Both blue and green loops only wind once to close the path.
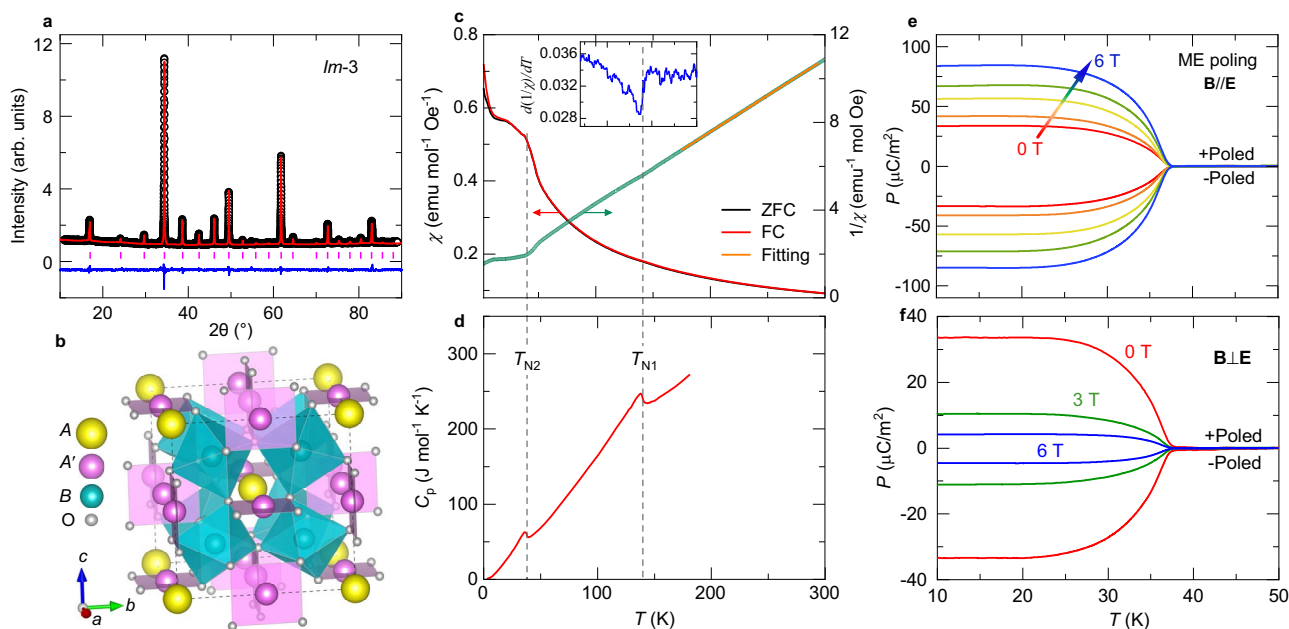
Fig. 2 Structure characterization, magnetic, specific heat and polarization measurements for TMCO. a XRD pattern measured at room temperature and the Rietveld refinement results. The observed (black circles), calculated (red line), and difference (blue line) values are shown. The ticks indicate the allowed Bragg reflections with space group Im-3. **b** Crystal structure of A-site ordered perovskite $AA'_3B_4O_{12}$ with Im-3 symmetry. **c** Temperature dependence of magnetic susceptibility χ measured at 0.1 T and its inverse χ^{-1}. Both zero-field-cooling (ZFC) and field-cooling (FC) modes were adopted to measure χ. The yellow line shows the Curie–Weiss fitting above 175 K. The fitted effective moment μ_{eff} (15.52 μ_B f.u.$^{-1}$) is comparable to the theoretical value (15.04 μ_B f.u.$^{-1}$) by considering the contribution from Tb^{3+}, Mn^{3+} and Cr^{3+} ions. The inset shows the derivative of inverse susceptibility versus temperature. **d** Temperature dependence of specific heat C_p measured at zero field. **e, f** Temperature dependent polarization P after poling the sample under an electric field ($= E_{pole}$) and different magnetic fields **B**, where **B** was not removed until the temperature increased to 50 K. For **B**//**E** and **B**⊥**E** configurations, both +Poled and -Poled conditions were measured.

topological properties as a mapping between the spin vector space and electric dipole vector space. Although some structurally and ferroelectrically coupled vortex domain patterns have been observed in hexagonal RMnO$_3$ (R = rare earth or Y, In) and BiFeO$_3$[27,33], spin-dependent topological multiferroics remain to be elucidated, the topological ME effects with versatile controls of **P** by **B** or **M** by **E** also need to be studied. Here, in A-site ordered cubic perovskites AMn$_3$Cr$_4$O$_{12}$ with high lattice symmetry, we discovered that the set of spin-induced ferroelectric polarizations can be described by a non-orientable Roman surface, as deduced through a 3D symmetry analysis. Various angle-dependent **P** oscillations under different magnetic fields were observed and can be understood based on the changes in the local topological structure and symmetry of the magnetism.

Results

Crystal structure of TbMn$_3$Cr$_4$O$_{12}$. To prove the high cubic symmetry of synthesized TbMn$_3$Cr$_4$O$_{12}$ (TMCO) at room temperature, we measured its powder X-ray diffraction (XRD) pattern and performed the Rietveld refinement (see Fig. 2a). The Rietveld analysis demonstrates that the compound crystallizes in an A-site ordered perovskite structure with the chemical formula $AA'_3B_4O_{12}$ (see Fig. 2b)[34,35]. The space group is cubic Im-3 with central symmetry, where Tb and Mn are 1:3 ordered at special Wyckoff sites $2a$ (0, 0, 0) and $6b$ (0, 0.5, 0.5), and Cr and O at special $8c$ (0.25, 0.25, 0.25) and $24g$ (x, y, 0) sites, respectively. Compared with a simple ABO$_3$ perovskite, the introduction of a transition metal into the A' site in the ordered $AA'_3B_4O_{12}$ perovskite results in the formation of square-coordinated A'O$_4$ units and heavily tilted BO$_6$ octahedra, as shown in Fig. 2b and described in detail in literatures[36,37]. Supplementary Table 2 lists the refined structural parameters of TMCO. According to the

refined Cr–O and Mn–O bond lengths, the bond valence sum calculations illustrate that the valence states of Mn and Cr are both close to +3, which agrees with the reported isostructural compound LaMn$_3$Cr$_4$O$_{12}$ (LMCO)[38]. Moreover, when the temperature was decreased to 5 K, there is no trace of the structural phase transition in TMCO (see Supplementary Fig. 2).

Magnetic properties of TbMn$_3$Cr$_4$O$_{12}$. Figure 2c, d shows the temperature dependence of the magnetic susceptibility and specific heat of TMCO, respectively. With the temperature decreasing to $T_{N1} \approx 136$ K, a sharp λ-type anomaly is observed in the specific heat, suggesting the occurrence of a second-order long-range magnetic phase transition. Moreover, the derivative of the inverse susceptibility displays a variation at T_{N1} (inset of Fig. 2c). Further, upon cooling to $T_{N2} \approx 36$ K, both the susceptibility and specific heat show a clear anomaly, illustrating a second long-range magnetic transition. Below T_{N2}, the specific heat does not show any visible anomaly, indicating the absence of spin ordering of Tb^{3+} at temperatures down to 2 K. The inverse susceptibility above 175 K follows the Curie–Weiss law (Fig. 2c). The fitted Weiss temperature of −28.0 K is indicative of antiferromagnetic (AFM) interactions. The linear isothermal magnetization behaviors within ±2 T further confirm the AFM orders occurring at T_{N1} and T_{N2} (see Supplementary Fig. 3a). However, at higher fields, a metamagnetic transition occurs near 2.5 T at temperatures below $T_{N1} \approx 136$ K, as demonstrated by the field derivative of magnetization, indicating field-induced variation in spin alignment (Supplementary Fig. 3b). Similar to LMCO[38], at zero field, the B-site Cr^{3+} spins are antiferromagnetically ordered in a collinear G-type fashion at T_{N1}; the A'-site Mn^{3+} sublattice experiences another G-type AFM ordering at T_{N2} in the current TMCO. The total spin structure, composed of Cr^{3+} and Mn^{3+}

magnetic sublattices with spin moments along the [111] direction, forms a type-II polar magnetic point group of $31'$, which breaks the space inversion symmetry. Therefore, a spin-induced ferroelectric phase transition is expected to occur at T_{N2}.

Spin-induced ferroelectric polarization in TbMn$_3$Cr$_4$O$_{12}$. Corresponding to the AFM phase transition, a frequency-independent dielectric peak is observed at $T_{N2} \approx 36$ K in TMCO, whereas no dielectric anomaly emerges at T_{N1} (Supplementary Fig. 4a, b). When magnetic field **B** and electric field **E** are simultaneously applied to measure the dielectric constant, an apparent anisotropic behavior can be observed. Specifically, a sharp dielectric peak is always observed with **B** up to 9 T for **B**//**E** (Supplementary Fig. 4c). By contrast, **B** significantly suppresses the dielectric peak in the **B**⊥**E** configuration, whereas the dielectric anomaly nearly disappears at 6 T (Supplementary Fig. 4d). These results strongly suggest that spin-induced ferroelectric polarization also shows distinctive responses to external magnetic fields along the parallel and perpendicular configurations in TMCO[38]. Furthermore, when the pyroelectric current I_p was measured to obtain temperature-dependent polarization, a sharp ferroelectric phase transition was observed at T_{N2} (Fig. 2e), as expected from the formation of the polar magnetic point group mentioned earlier. The polarization is reversible without changing the magnitude if the sign of the poling electric field (E_{pole}) is reversed, further confirming the spin-induced ferroelectric phase transition in TMCO. Similar to the dielectric measurements, applying a magnetic field with a **B**//**E** configuration can significantly enhance the polarization from 33.3 μC/m² at 0 T to 84.4 μC/m² at 6 T (Fig. 2e). However, in the **B**⊥**E** configuration, the spin-induced polarization is suppressed to 10.7 μC/m² at **B** = 3 T, and only 4.51 μC/m² at **B** = 6 T (Fig. 2f). All experimental results indicate that TMCO has the same crystal and magnetic structures as LMCO[38].

General relationship between spin and polarization directions of AMn$_3$Cr$_4$O$_{12}$. Based on the crystal and spin structure symmetry analyses, the peculiar ME multiferroicity of AMn$_3$Cr$_4$O$_{12}$ can be described through the topological Roman surface **RP²**. As mentioned, both TMCO and LMCO have a cubic crystal symmetry of $Im\text{-}3$, where inversion centers are located on each Cr atom, with four three-fold rotation axes along four body diagonals and three mirror planes perpendicular to the three Cartesian axes (Fig. 3a). The total magnetic structure composed of Cr^{3+} spins (we use Néel vector $\mathbf{S}_{Cr}$ to trace the coherent motion of spins in the AFM ordering of Cr ions) and Mn^{3+} spins (Néel vector $\mathbf{S}_{Mn}$) forms a polar magnetic point group $31'$ with $\mathbf{S}_{Mn}$//$\mathbf{S}_{Cr}$//[111] (see Fig. 3a). According to the proposed anisotropic symmetric exchange mechanism[39] (see Supplementary Section 1) originating from spin–orbit coupling, such a special spin structure induces polarization **P** along the [111] direction. To describe a general relationship between the spin and polarization directions, we assign $\mathbf{S}_{Cr} = (\mu_{Cr}, \theta, \varphi)$ and $\mathbf{S}_{Mn} = (\mu_{Mn}, \theta, \varphi)$. Both are on sphere $\mathbf{S}^2$ (Fig. 3a and b), where $\theta \in [0, \pi]$ and $\varphi \in [-\pi, \pi]$ with fixed magnitudes μ_{Cr} and μ_{Mn}. Thus, the polarization **P** is expressed as a function of spins $\mathbf{P}(\mathbf{S}_{Mn}, \mathbf{S}_{Cr}) = \mathbf{P}(\theta, \varphi)$ mapping from $\mathbf{S}^2$ to $\mathbf{RP}^2$. Based on strict symmetrical analysis[40], as described in Supplementary Sections 2 and 3, we see that $\mathbf{P}(\theta, \varphi)$ has the following form:

$$\mathbf{P} = \beta\mu_{Cr}\mu_{Mn}\Omega[\sin(2\theta)\sin(\varphi), \ \sin(2\theta)\cos(\varphi), \ \sin^2\theta\,\sin(2\varphi)]$$
$$(2)$$

where the coefficients β and Ω depend on temperature and crystal properties, respectively. The polarization vector $\mathbf{P}(\theta, \varphi) = (P_a, P_b, P_c)$
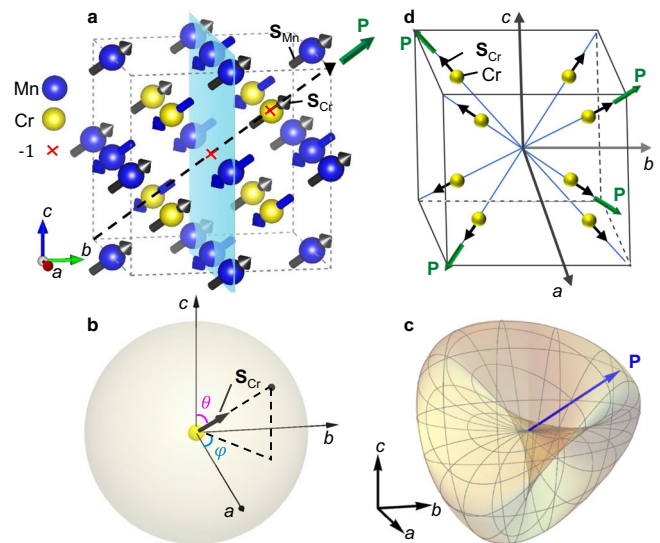
Fig. 3 Crystal, magnetic, and ferroelectric structures in AMn$_3$Cr$_4$O$_{12}$. **a** Crystal and spin configurations where Cr and Mn atoms are presented in yellow and blue, respectively, and O atoms are omitted for clarity. The lattice symmetries of AMn$_3$Cr$_4$O$_{12}$: two space inversions $\bar{1}$ located at the center and at the Cr atom, one of the mirror planes (see the light-blue plane), and one of the three-fold rotation axes (see the dash line) are indicated. All spins composed of Mn and Cr magnetic sublattices are parallel or antiparallel to the [111] direction. Antiferromagnetic sublattices of Cr and Mn are denoted by Néel vectors $\mathbf{S}_{Cr}$ and $\mathbf{S}_{Mn}$, respectively, and the induced polarization **P** is shown by the arrow in green. **b** Orientation of $\mathbf{S}_{Cr}$ is represented in spherical coordinates ($\mu_{Cr}, \theta, \varphi$). **c** Complete set of allowed spin-induced **P** vectors in three dimensions is a Roman surface when the magnetic structure shown in **a** coherently rotates on a sphere in **b**. **d** Distribution of **P** vectors along four of the eight diagonal directions. The yellow sphere and the black arrow denote the Cr atom and its spin moment. $\mathbf{S}_{Mn}$ is always parallel to $\mathbf{S}_{Cr}$, and it is not shown for clarity. Thus, AFM configuration composed of Mn and Cr sublattices is indicated by $\mathbf{S}_{Cr}$. The black cube represents the crystal unit cell.

is rewritten using an analytical equation as follows:

$$P_a^2P_b^2 + P_a^2P_c^2 + P_b^2P_c^2 - 2\beta\mu_{Cr}\mu_{Mn}\Omega P_aP_bP_c = 0 \qquad (3)$$

Equation (3) is a specific case of Eq. (1) with $x = P_a$, $y = P_b$, $z = P_c$, and $\delta = 2\beta\mu_{Cr}\mu_{Mn}\Omega$. This result indicates that the induced **P** vectors in AMn$_3$Cr$_4$O$_{12}$ may constitute a non-orientable Roman surface **RP²** (see Fig. 3c).

In this cubic multiferroic family, the collinear G-type AFM locks the Néel vectors $\mathbf{S}_{Mn}$ and $\mathbf{S}_{Cr}$ in parallel; they pass through all eight equivalent diagonal directions coherently (see Supplementary Section 3 for details). Only four of the eight diagonal directions are allowed for the polarization **P** vectors, which form a regular tetrahedron and agrees with the tetrahedral symmetry of the Roman surface (Fig. 3d). Note that there is another AFM configuration with $\mathbf{S}_{Mn}$ antiparallel to $\mathbf{S}_{Cr}$ (see Supplementary Fig. 5), which leads to a set of polarization vectors **P** forming a Roman surface with negative δ and having similar features as the positive one discussed here.

Topological multiferroicity of AMn$_3$Cr$_4$O$_{12}$. The spin–polarization relationship in cubic perovskites AMn$_3$Cr$_4$O$_{12}$ leads to topological multiferroicity owing to the topological and symmetry properties of the Roman surface discussed earlier. The mapping from $\mathbf{S}^2$ to $\mathbf{RP}^2$ covers the Roman surface twice, because $\mathbf{S}_{Cr}$ and $-\mathbf{S}_{Cr}$ induce identical **P** vectors. This is similar to the spin–momentum locking
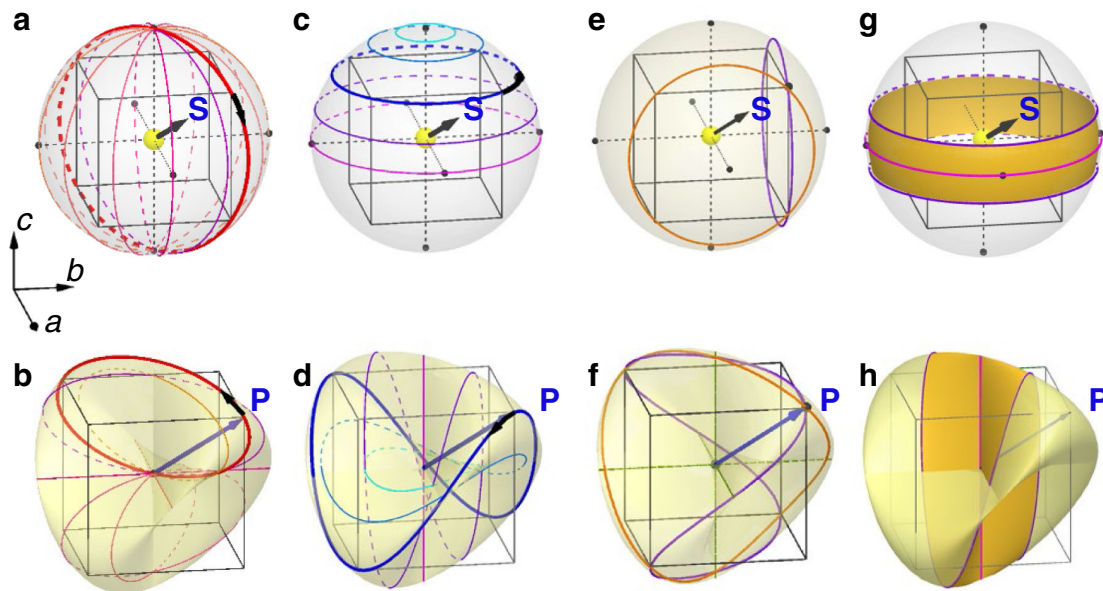
Fig. 4 Various loops on a sphere of Néel vectors (top panels) and the induced fundamental polarization trajectories on Roman surface (bottom panels). a Longitudinal (fixed φ) path of the Néel vector rotation mode with a series of selected φ values and continuously varying $\theta \in [0, 2\pi]$. **b** Trajectories of **P** induced by loops in **a** with the same color. **c** Latitudinal (fixed θ) Néel vector rotation mode with a series of selected θ values and continuously varying $\varphi \in [-\pi, \pi]$. **d** Trajectories of **P** induced by loops in **c** with the same color. The six special points, the intersections between sphere and a-, b- and c-axis, are illustrated in black point in **a** and **c**. The thicker lines in **a** and **c** represent two special cases where four diagonal directions are passed through; the resultant trajectories of **P** are indicated by the thicker lines in **b** and **d**, respectively. Rotation directions of S_{Cr} and **P** are indicated by black arrows toward opposite directions away from [111] direction. The animations of **a**–**d** are shown in Supplementary Videos 1–3. **e** Two closed loops winding the a and b axes once are shown in orange and purple, respectively. **f** Two closed trajectories of **P** on the Roman surface are induced by the loops in **e**. The loops with $W_a = 1$ are in orange and those with $W_b = 1$ are in purple. **g**, **h** A band included in the equator of the Néel vector sphere **g** is mapped to **h**, a self-crossed Möbius strip as a part of the Roman surface. The residual upper and lower caps are mapped to a disc on the Roman surface simultaneously. All the loops in **b**, **d**, and **f** are fundamental loops defined in Fig. 1c.

effect on the Fermi surface enclosing Weyl nodes. The Hamiltonian around the Weyl node maps the momentum space (Fermi sphere, S^2) to the spin space (another sphere called the Bloch sphere). If the enclosed Weyl node have a topological charge of one or two, the momentum moves around the node once and the spin rotates once or twice, respectively. The relative rotational directions of the momentum and spin are determined by the sign of the charge[41]. In this sense, a closed evolution loop of Néel vectors S_{Cr} on the sphere may map to a non-trivial path of the **P** vector on the Roman surface, showing topological ME effects.

The red loop in Fig. 1c passes through the triple point of the Roman surface twice, where polarization **P** = 0. This can be induced by the evolution of S_{Cr} on sphere S^2, which includes six special points where the sphere intersects the a-, b-, and c-axis (see Fig. 4a). For a longitudinal great circle of the sphere with φ fixed, as Fig. 4a shows, S_{Cr} passes through the special points twice (the north and south poles) if φ is not 0, $\pi/2$, π, or $3\pi/2$. This results in a double-winding elliptical trajectory of the **P** vector passing through the triple point twice (see Fig. 4b and Supplementary Video 1). The induced **P** rotates twice, whereas S_{Cr} travels through one loop. When $\varphi = 0$, $\pi/2$, π, or $3\pi/2$, the trajectories of **P** collapse to the double lines and pass through special points four times (see Fig. 4b and Supplementary Videos 1 and 2). It is observed that only the magnitude of **P** vibrates, and the period is twice the loop evolution of S_{Cr}.

When the Néel vectors evolve along the latitudinal parallels with the polar axis being the c-axis and a fixed θ value (θ is not 0 or $\pi/2$), as Fig. 4c shows, the induced saddle-like trajectory of **P** on the Roman surface only winds around the c-axis (Fig. 4d and Supplementary Video 3). This trajectory of **P** is nontrivial, in the sense that $W_c = 1$. The projection onto the ab-plane is a circle.

The rotation direction, clockwise or counterclockwise, of the projection of the **P** vector on the circle is opposite to that of the Néel vector. Note that the rotation period of the **P** vector is the same as that of S_{Cr}, instead of double that in the cases shown in Fig. 4b. Similarly, when S_{Cr} winds around either the a- or b-axis once, the corresponding **P** vector loop on the Roman surface is characterized by $W_a = 1$ or $W_b = 1$, respectively, as indicated in Fig. 4e and f. Notably, nonzero W_i corresponds to the component of the **P** vector perpendicular to the i-axis that reverses W_i times during one loop evolution. The green circle in Fig. 1c is topologically trivial with zero values of W_i. It can be mapped from a loop on the S_{Cr} sphere that satisfies these conditions: there is no special point being wound, and $-S_{Cr}$ will not be passed by for any S_{Cr} on the path. To reveal the underlying topological origins of the double-winding and single-winding paths in Figs. 4b, d, and 1c, we mapped a strip composed of the neighborhoods of the equator and itself on the spin sphere (Fig. 4g) to a Möbius strip (Fig. 4h) on the Roman surface. Meanwhile, the residual upper and lower caps on the sphere are mapped to a saddle-like disc. Thus, according to the orientable and non-orientable nature of the disc and the Möbius strip, their paths on them will wind once and twice, respectively, to form a closed loop.

Topological ME effects in AMn$_3$Cr$_4$O$_{12}$. We experimentally present the topological ME effects in TMCO and LMCO polycrystalline samples with identical crystal and spin structures. To define the relative orientations of **E** and **B** on the polycrystalline sample, we defined a local x, y, and z coordinate system (see Fig. 5a). First, the samples were cooled down to 10 K under $E_{pole}//y$ at zero **B**. Subsequently, we removed the electric field E_{pole} and measured the **B**-dependent **P** by sweeping **B** in either the **B**//y or
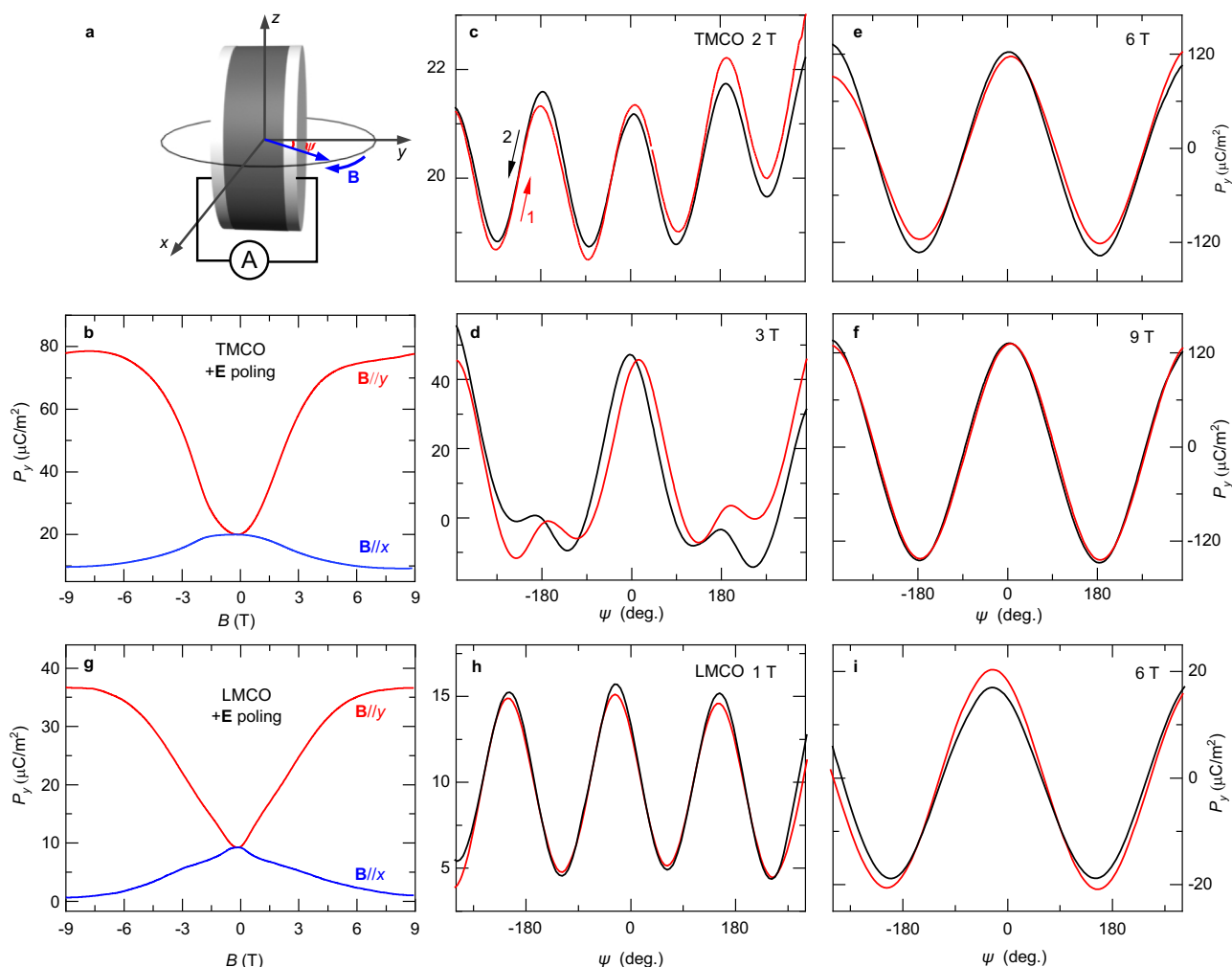
Fig. 5 Polarization variations under sweeping and rotating B at 10 K for TMCO and LMCO. a Schematic illustration of measurements for magnetoelectric current under rotating **B** within the xy-plane; ψ denotes the angle between **B** and the y-direction. **b**, **g** Magnetic-field-dependent P_y at $T = 10$ K after $+$**E** poling for **B**//**E** and **B**⊥**E** configurations of TMCO and LMCO, respectively. P_y is defined as the component of **P** along the y-axis. **c–f** ψ-dependent polarization of TMCO at **B** $= 2$ T **c**, 3 T **d**, 6 T **e**, and 9 T **f**. The red and black arrows indicate an increase or decrease in angle, respectively. **h**, **i** ψ-dependent polarization of LMCO at **B** $= 1$ T **h** and 6 T **i**. All polarizations were integrated from the ME current as a function of time.

B//x configuration (Fig. 5a). In both configurations, quadratic ME effects were dominant in TMCO (Fig. 5b). This is consistent with the $31'$ point group with independent time-reversal symmetry, where a quadratic rather than a linear ME effect is allowed. To investigate the postulated topological ME effects in TMCO, rotating **B** was applied to continuously tune the orientation of the Néel vector S_{Cr}. The **B** direction dependence of P_y under a selected field-strength by changing ψ (initially $\psi = 0$ with **B**//y; Fig. 5c–f) was measured after electrical poling to 10 K. The ψ dependence of P_y exhibited double-angle sinusoidal modulation curves at **B** within ~2 T without changing the sign (Fig. 5c). This is a direct manifestation of the intrinsic quadratic ME behavior in this system. Based on Monte Carlo simulations, we find that under a relatively small rotating **B** without inducing metamagnetic transition, the Néel vector S_{Cr} will slightly tilt away from the diagonal direction, leading to a topologically trivial path on the sphere. However, it is to be noted that S_{Cr} itself is double period of rotating **B** (see Supplementary Section 4 and Supplementary Fig. 6a). Moreover, the resulting loop of the **P** vector on the Roman surface is a small perturbation to its original position, with zero values of W_i (Supplementary Fig. 6b), as exemplified by the green loop in Fig. 1c. Therefore, S_{Cr} travels along a green-type path twice when **B** rotates 360° (Supplementary Fig. 7). This

results in a double winding of the loop on the Roman surface, which is consistent with the experimentally observed double-angle sinusoidal modulation of P_y for small **B**, indicating trivial mapping from S_{Cr} to **P** along the green loop. Additionally, under applied magnetic field, **B** will change the orientation of antiferromagnetic axis and induce a small ferromagnetic component simultaneously. The Zeeman energy and antiferromagnetic exchange energy will compete with each other. The AFM components of spins tend to align normally with the direction of **B** while the induced ferromagnetic components point towards the **B** direction. This is also consistent with our Monte Carlo simulations under a small **B** in Supplementary Figs. 6a and 7a where **B**// b ($\Phi = 90°$) leads to a significant weakening of S_{Cr}^y in spins.

For **B** values greater than 3 T, a sinusoidal P_y variation appeared, owing to the metamagnetic transition occurring at a critical field of approximately 2.5 T (Supplementary Fig. 3b). At **B** $= 6$ and 9 T, the P_y value can be reversed with pure sinusoidal behavior (Fig. 5e, f). The energy barrier of magnetic anisotropy in the diagonal directions can be overcome by increasing the Zeeman energy, and a spin-flop transition occurs at a larger rotating **B** (> 3 T) to induce a nontrivial loop of the Néel vector on the sphere. The loop of the Néel vector winds its principal axis under a sufficiently high **B**, which induces a **P** vector loop with

one of $W_i = 1$ ($i = a, b, c$) on the Roman surface. This leads to a reversal of the **P** components perpendicular to the i-axis, as the blue loop in Fig. 1c. Thus, the pure sinusoidal **P** behavior at 6 T and 9 T in TMCO can be understood.

As Fig. 5d shows, both single- and double-angle sinusoidal P_y features coexist at **B** = 3 T with clear hysteresis behavior. $P = 0$ values have been reached multiple times in one period. There is a possibility that the loops of the Néel vector pass through some of the crystal axes, and some naught **P** values occur during a 360° rotation of **B**, as in the red loop in Fig. 1c. Note that owing to the polycrystalline specimens used in the experiments, it is impossible to determine the detailed grain configurations or **P** rotating paths of each grain for the TMCO. In isostructural LMCO, all the aforementioned ME behaviors can be reproduced (Fig. 5g–i), indicating the universality of these phenomena in the cubic multiferroic perovskite family of $AMn_3Cr_4O_{12}$.

Discussion

We propose that topological nontrivial rotation of **P** is realized in the multiferroic domain walls of $AMn_3Cr_4O_{12}$ without an external magnetic field. As Supplementary Fig. 8 shows, there are three types of multiferroic domains with S_{Mn} parallel to S_{Cr}, considering that the Néel vectors prefer eight diagonal directions, i.e., 71°, 109°, and 180°. AFM domains are induced at 109°, 109°, and 360°. In particular, ferroelectric domains are induced at 360°. The ferroelectric domain wall represents a half winding of the Möbius strip since a 180° rotation of S_{Cr} leads to one loop of **P** and a mirror reflected on the Roman surface (Supplementary Fig. 8c). This type of multiferroic domain wall cannot be destroyed by an external electric field because the polarizations in two neighboring ferroelectric domains can be coherently aligned in the direction of the electric field; whereas, the related AFM configurations will always be opposite. This would be a type of topological object unique in $AMn_3Cr_4O_{12}$, which deserves further investigation. Moreover, it is worthy to note that the magnetic skyrmion of Cu_2OSeO_3[42] may also map the induced polarization as a complete Roman surface owing to the similar polarization distribution to that of $AMn_3Cr_4O_{12}$.

In summary, we investigated the unusual spin–polarization relationship in A-site-ordered cubic perovskite oxides AMn_3-Cr_4O_{12}. The uncommon polarization occurring in the cubic system is coupled with the inversion symmetry breaking caused by G-type collinear AFM ordering composed of Mn^{3+} and Cr^{3+} magnetic sublattices. We discovered that the ME behavior, namely, the mapping from spin to the induced polarization, can be considered as a physical entity realizing the Roman surface, which is a non-orientable 2D manifold. This is different from other topological objects defined on orientable manifolds, such as Chern insulators defined on a torus and skyrmions defined on a sphere. The non-orientability of the Roman surface leads to topological ME effects depending on the evolution of the path. In our experiments, different types of angle-dependent polarization are observed in polycrystalline TMCO and LMCO under different magnetic fields. The evolution paths of the spin vectors are controlled by a magnetic field, and the induced **P** evolves along orientable or non-orientable surfaces to show different topological properties. This study provides an interesting fact that topology has a close and deep relationship with the physical world, opening up an avenue to achieve more topological objects from an orientable manifold to a non-orientable manifold.

Methods

Materials synthesis. Polycrystalline TMCO was synthesized via a solid-state reaction at a high temperature and high pressure. Tb_4O_7, MnO, Cr_2O_3, and Mn_2O_3 powders were used as the starting materials at a molar ratio of 1:2:8:5. The finely mixed reactants were packed into a gold capsule 4.0 mm in length and 2.8 mm in

diameter and then treated at 1300 K and 7 GPa for 30 min on a cubic-anvil-type high-pressure apparatus.

Structural determination. Powder XRD analysis was performed using a Huber diffractometer with Cu Kα1 radiation at 40 kV and 30 mA. Diffraction data were collected in the 2θ angle range of 10° to 100°. A program from the general structure analysis system was used to refine the XRD data using the Rietveld method[43]. Raman spectra were collected on a T64000 spectrometer using a liquid-nitrogen-cooled charge-coupled device. Volume Bragg gratings of 600 G and 488 nm laser were used to measure the spectra.

Magnetic characterization. The magnetic susceptibility and magnetization were measured using a superconducting quantum interference device magnetometer (Quantum Design, MPMS-7T). Zero-field-cooling and field-cooling modes were adopted to measure the susceptibility at a magnetic field of 0.1 T. Magnetization was measured between −14 T and 14 T at selected temperatures. Specific heat measurements were performed using a physical property measurement system (Quantum Design, PPMS-9T) at zero field.

Electric measurements. A hard disk-shaped piece 2.0 mm in diameter and 0.2 mm in thickness was used to measure the relative dielectric constant on an Agilent-4980A LCR meter. Silver paste was used as the electrodes. Subsequently, the sample was used to measure the pyroelectric current and isothermal polarized current under different magnetic fields using a Keithley 6517B electrometer. To measure the pyroelectric current for TMCO, the sample was poled with an electric field of $E_{pole} = \pm 11.7$ kV/cm and a magnetic field from 50 K to 10 K. Then, the electric field was removed. After waiting for 30 min in an electric short circuit, pyroelectric current data were collected at temperatures ranging from 10 K to 50 K at a speed of 2 K/min. Polarization P was obtained by integrating the current data as a function of time. The polycrystalline sample LMCO was also prepared in a disk-shaped piece with 0.23 mm in thickness to measure the polarization. In the measurements of magnetic-field dependent and angle-dependent polarizations, the polycrystalline sample was poled by an electric field of 8.33 kV/cm for TMCO and 8.68 kV/cm for LMCO down to 10 K. After the electrical poling procedure, different magnetic field was applied to the sample to measure the isothermal polarized current; then, the magnetic-field-dependent polarization or angle-dependent polarization was obtained by integrating the current.

Data availability
The data supporting this study's findings are available from the corresponding authors upon reasonable request.

Code availability
The codes in this study are available from the corresponding authors upon reasonable request.

References
1. Klitzing, K. V., Dorda, G. & Pepper, M. New method for high-accuracy determination of the fine-structure constant based on quantized hall resistance. *Phys. Rev. Lett.* **45**, 494–497 (1980).
2. Weng, H., Yu, R., Hu, X., Dai, X. & Fang, Z. Quantum anomalous Hall effect and related topological electronic states. *Adv. Phys.* **64**, 227–282 (2015).
3. Hasan, M. Z. & Kane, C. L. Colloquium: topological insulators. *Rev. Mod. Phys.* **82**, 3045–3067 (2010).
4. Qi, X.-L. & Zhang, S.-C. Topological insulators and superconductors. *Rev. Mod. Phys.* **83**, 1057–1110 (2011).
5. Armitage, N. P., Mele, E. J. & Vishwanath, A. Weyl and Dirac semimetals in three-dimensional solids. *Rev. Mod. Phys.* **90**, 015001 (2018).
6. Thouless, D. J., Kohmoto, M., Nightingale, M. P. & den Nijs, M. Quantized Hall conductance in a two-dimensional periodic potential. *Phys. Rev. Lett.* **49**, 405–408 (1982).
7. Berry, M. V. Quantal phase factors accompanying adiabatic changes. *Proc. R. Soc. Lond. Ser. A* **392**, 45 (1984).
8. Kane, C. L. & Mele, E. J. Z_2 topological order and the quantum spin Hall effect. *Phys. Rev. Lett.* **95**, 146802 (2005).

9. Song, Z., Zhang, T., Fang, Z. & Fang, C. Quantitative mappings between symmetry and topology in solids. *Nat. Commun.* **9**, 3530 (2018).
10. Ahn, J., Park, S. & Yang, B.-J. Failure of Nielsen-Ninomiya theorem and fragile topology in two-dimensional systems with space-time inversion symmetry: application to twisted bilayer graphene at magic angle. *Phys. Rev. X* **9**, 021013 (2019).
11. Bouhon, A. et al. Non-Abelian reciprocal braiding of Weyl points and its manifestation in ZrTe. *Nat. Phys.* **16**, 1137–1143 (2020).
12. Mühlbauer, S. et al. Skyrmion lattice in a chiral magnet. *Science* **323**, 915–919 (2009).
13. Yu, X. Z. et al. Real-space observation of a two-dimensional skyrmion crystal. *Nature* **465**, 901–904 (2010).
14. Das, S. et al. Observation of room-temperature polar skyrmions. *Nature* **568**, 368–372 (2019).
15. Wang, Y. J. et al. Polar meron lattice in strained oxide ferroelectrics. *Nat. Mater.* **19**, 881–886 (2020).
16. Nagaosa, N. & Tokura, Y. Topological properties and dynamics of magnetic skyrmions. *Nat. Nanotechnol.* **8**, 899–911 (2013).
17. Tanda, S. et al. A Möbius strip of single crystals. *Nature* **417**, 397–398 (2002).
18. Han, D., Pal, S., Liu, Y. & Yan, H. Folding and cutting DNA into reconfigurable topological nanostructures. *Nat. Nanotechnol.* **5**, 712–717 (2010).
19. Young, S. M. & Kane, C. L. Dirac semimetals in two dimensions. *Phys. Rev. Lett.* **115**, 126803 (2015).
20. Wang, Z., Alexandradinata, A., Cava, R. J. & Bernevig, B. A. Hourglass fermions. *Nature* **532**, 189–194 (2016).
21. Zhang, R. X., Wu, F., & Das Sarma, S. Möbius insulator and higher-order topology in $MnBi_{2n}Te_{3n+1}$. *Phys. Rev. Lett.* **124**, 136407 (2020).
22. Li, T. et al. Acoustic Möbius insulators from projective symmetry. *Phys. Rev. Lett.* **128**, 116803 (2022).
23. Xue, H. et al. Projectively enriched symmetry and topology in acoustic crystals. *Phys. Rev. Lett.* **128**, 116802 (2022).
24. Bartolo, D. & Carpentier, D. Topological elasticity of nonorientable ribbons. *Phys. Rev. X* **9**, 041058 (2019).
25. Hilbert, D. & Cohn-Vossen, S. *Geometry and the Imagination* (Chelsea, New York, 1999).
26. Gray, A. *Modern Differential Geometry of Curves and Surfaces with Mathematica*. 2nd ed (CRC Press, Boca Raton, 1997).
27. Dong, S., Liu, J.-M., Cheong, S.-W. & Ren, Z. Multiferroic materials and magnetoelectric physics: Symmetry, entanglement, excitation, and topology. *Adv. Phys.* **64**, 519–626 (2015).
28. O'Dell, T. H. *The Electrodynamics of Magneto-electric Media*. (North-Holland, Amsterdam, 1970).
29. Jia, C., Onoda, S., Nagaosa, N. & Han, J. H. Bond electronic polarization induced by spin. *Phys. Rev. B* **74**, 224444 (2006).
30. Sergienko, I. A. & Dagotto, E. Role of the Dzyaloshinskii-Moriya interaction in multiferroic perovskites. *Phys. Rev. B* **73**, 094434 (2006).
31. Sergienko, I. A., Sen, C. & Dagotto, E. Ferroelectricity in the magnetic E-phase of orthorhombic perovskites. *Phys. Rev. Lett.* **97**, 227204 (2006).
32. Murakawa, H., Onose, Y., Miyahara, S., Furukawa, N. & Tokura, Y. Ferroelectricity induced by spin-dependent metal-ligand hybridization in $Ba_2CoGe_2O_7$. *Phys. Rev. Lett.* **105**, 137202 (2010).
33. Lu, C., Wu, M., Lin, L. & Liu, J.-M. Single-phase multiferroics: New materials, phenomena, and physics. *Natl Sci. Rev.* **6**, 653–668 (2019).
34. Shimakawa, Y. A-site-ordered perovskites with intriguing physical properties. *Inorg. Chem.* **47**, 8562–8570 (2008).
35. Long, Y. W. et al. Temperature-induced A-B intersite charge transfer in an A-site-ordered $LaCu_3Fe_4O_{12}$ perovskite. *Nature* **458**, 60–63 (2009).
36. Long, Y. A-site ordered quadruple perovskite oxides $AA'_3B_4O_{12}$. *Chin. Phys. B* **25**, 078108 (2016).
37. Long, Y. & Shimakawa, Y. Intermetallic charge transfer between A-site Cu and B-site Fe in A-site-ordered double perovskites. *N. J. Phys.* **12**, 063029 (2010).
38. Wang, X. et al. Observation of magnetoelectric multiferroicity in a cubic perovskite system: $LaMn_3Cr_4O_{12}$. *Phys. Rev. Lett.* **115**, 087601 (2015).
39. Feng, J. S. & Xiang, H. J. Anisotropic symmetric exchange as a new mechanism for multiferroicity. *Phys. Rev. B* **93**, 174416 (2016).
40. Chai, Y. S., Chun, S. H., Cong, J. Z. & Kim, K. H. Magnetoelectricity in multiferroic hexaferrites as understood by crystal symmetry analyses. *Phys. Rev. B* **98**, 104416 (2018).
41. Xu, G., Weng, H., Wang, Z., Dai, X. & Fang, Z. Chern semimetal and the quantized anomalous Hall effect in $HgCr_2Se_4$. *Phys. Rev. Lett.* **107**, 186806 (2011).
42. Seki, S., Ishiwata, S. & Tokura, Y. Magnetoelectric nature of skyrmions in a chiral magnetic insulator Cu_2OSeO_3. *Phys. Rev. B* **86**, 060403 (2012).
43. Larson, A. C. & von Dreele, R. B. General Structure Analysis System (GSAS). Report No. LAUR 86-748 (Los Alamos National Laboratory, 1994).

Author contributions

Y.L., Y.C., and H.W. conceived and led this project. M.P., X.C., and Y.C. performed the theoretical calculations. G.L., X.Ye, B.Z., and J.G. synthesized the samples. G.L., L.Zhou, X.S., and X.M. performed dielectric constant and polarization measurements and data analysis. Z.L., S.Q., L.Zhao, and X.Yu performed the structural and magnetic measurements. G.L., M.P., H.W., Y.C., and Y.L. wrote the manuscript. All the authors discussed the results and commented on the manuscript.

Competing interests

The authors declare no competing interests.

Additional information

Supplementary information The online version contains supplementary material available at https://doi.org/10.1038/s41467-022-29764-w.

Correspondence and requests for materials should be addressed to Yisheng Chai , Hongming Weng or Youwen Long.

Peer review information *Nature Communications* thanks the other anonymous reviewer(s) for their contribution to the peer review of this work. Peer review reports are available.

Reprints and permission information is available at http://www.nature.com/reprints

Publisher's note Springer Nature remains neutral with regard to jurisdictional claims in published maps and institutional affiliations.